



1                   **An improved dynamic bidirectional coupled hydrologic-**  
2                   **hydrodynamic model for efficient flood inundation prediction**

3                   Yanxia Shen, Zhenduo Zhu, Qi Zhou, Chunbo Jiang\*

4                   State Key Laboratory of Hydrosience and Engineering, Department of Hydraulic  
5                   Engineering, Tsinghua University, Beijing, 100084, China

6   **Abstract:** To improve computational efficiency while maintaining numerical accuracy,  
7   coupled hydrologic-hydrodynamic models based on non-uniform grids are used for  
8   flood inundation prediction. In those models, a hydrodynamic model using a fine grid  
9   can be applied for flood-prone areas, and a hydrologic model using a coarse grid can  
10   be used for the rest of the areas. However, it is challenging to deal with the separation  
11   and interface between the two types of areas because the boundaries of the flood-prone  
12   areas are time-dependent. We present an improved Multigrid Dynamical Bidirectional  
13   Coupled hydrologic-hydrodynamic Model (IM-DBCM) with two major improvements:  
14   1) automated non-uniform mesh generation based on the  $D_\infty$  algorithm was  
15   implemented to identify the flood-prone areas where high-resolution inundation  
16   conditions are needed; 2) ghost cells and bilinear interpolation were implemented to  
17   improve numerical accuracy in interpolating variables between the coarse and fine grids.  
18   A hydrologic model, two-dimensional (2D) nonlinear reservoir (NLR) model was  
19   bidirectionally coupled with a 2D hydrodynamic model that solves the shallow water  
20   equations. Three cases were considered to demonstrate the effectiveness of the  
21   improvements. In all cases, the mesh generation algorithm was shown to efficiently and  
22   successfully generate high-resolution grids only in those flood-prone areas. Compared  
23   with the original M-DBCM (OM-DBCM), the new model had lower RMSEs and higher

---

\*Corresponding author: State Key Laboratory of Hydrosience and Engineering, Department of Hydraulic Engineering, Tsinghua University, Beijing, 100084, China  
Corresponding author: Tel: +8613581891886; E-mail address: jcb@tsinghua.edu.cn



24 NSEs, indicating that the proposed mesh generation and interpolation were reliable and  
25 stable. It can be adapted adequately to the real-life real flood evolution process in  
26 watersheds and provide practical and reliable solutions for rapid flood prediction.

27 **Key words:** Coupled hydrologic-hydrodynamic model; Multi-grid generation; Bilinear  
28 interpolation; Computational efficiency and accuracy; Flood simulation

## 29 **1 Introduction**

30 Floods are the most frequent natural disasters that seriously harm human health  
31 and economic growth. Numerical models are critical for predicting flooding processes  
32 to help prevent or mitigate the damaging effects of floods on people and communities  
33 (Bates, 2022). Coupled hydrologic-hydrodynamic models are widely used to translate  
34 the amount of rainfall obtained from weather forecasting models or rain gauge  
35 observations into surface inundation (Xia et al., 2019).

36 Coupled hydrologic-hydrodynamic models can be generally divided into two  
37 categories. The first category is full 2D hydrodynamic models (HM2D), where the 2D  
38 hydrodynamic model is used to simulate the overland flow (runoff routing and flood  
39 inundation), and only the runoff generation is calculated by the hydrologic model and  
40 added into the mass source term of the 2D hydrodynamic model (Singh et al., 2011;  
41 Garcia-Navarro et al., 2019; Hou et al., 2020; Costabile and Costanzo, 2021). The  
42 development and simulation of HM2D require high-resolution topographic data at the  
43 catchment scale and extensive computational time, which hinder their application in  
44 large-scale flood forecasting. A promising way to achieve computational speedups is  
45 execution in a massively parallel fashion on supercomputers (Noh et al., 2018; Kuffour  
46 et al., 2020) or graphic processing unit (GPU) (Kuffour et al., 2020; Ming et al., 2020;  
47 Morales-Hernández et al., 2021; Buttinger-Kreuzhuber et al., 2022). Besides the  
48 computational efficiency, the numerical stability of HM2D can be problematic,



49 especially in thin-layer water regions (Kim et al., 2012).

50 The second category of coupled hydrologic-hydrodynamic models uses  
51 hydrologic models for upland areas and hydrodynamic models for main channels and  
52 flood-prone areas, and the hydrologic model provides the discharge boundary for the  
53 hydrodynamic model (Hdeib et al., 2018; Munar et al., 2018; Shin et al., 2019; Gomes,  
54 et al., 2021). And therefore, this category can be more efficient and thus applied to  
55 large-scale studies. This category is further divided into one-way and two-way coupling  
56 models, according to whether the hydrodynamic model provides feedback to the  
57 hydrologic model.

58 In one-way coupling models, the hydrologic model is run first and independently  
59 from the hydrodynamic model. The hydrographs obtained from hydrologic models are  
60 used as an input for the hydrodynamic models in a fixed position (Schumann et al.,  
61 2013; Feistl et al., 2014; Choi and Mantilla, 2015; Bhola, 2018; Wing et al., 2019). This  
62 one-way flow information cannot capture the mutual interaction between runoff  
63 production and flood inundation, and the fixed interface is inconsistent with the actual  
64 flood process where the inflow discharge positions, flow path, and discharge values  
65 change with accumulating rainfall.

66 In two-way coupling models, the governing equations of the hydrologic and  
67 hydrodynamic models are solved simultaneously in each time step, with information at  
68 the shared interface updated and exchanged at each or several computational time steps.  
69 Most existing two-way models are the coupling of hydrologic and one-dimensional (1D)  
70 hydrodynamic models, such as the coupling of Mike SHE and Mike 11, SWMM  
71 (Thompson et al., 2004; Laganier et al., 2013; Rossman, 2015; Chalkidis et al., 2016).  
72 The application of 1D modeling of overland flow is limited when developing precise  
73 and reliable flood maps in 2D inundation regions. Jiang et al. (2021) proposed a



74 dynamic bidirectional coupling model (DBCM), where the hydrologic and 2D  
75 hydrodynamic models were solved synchronously in each time step. The hydrologic  
76 and 2D hydrodynamic models are coupled through a coupling moving interface (CMI),  
77 and the inflow discharge positions and flow path change with accumulating rainfall, it  
78 had better numerical accuracy than the one-way coupling models.

79 However, because uniform grids were adopted in DBCM, high-resolution  
80 simulations in a large domain inevitably involved numerous computational nodes and  
81 substantially increased the computational cost. An essential consideration to reduce  
82 computational time is mesh coarsening (Caviedes-Voullième et al., 2012). Adaptive  
83 mesh refinement (AMR) has been used to optimize the grid resolution during flood  
84 simulations (Donat et al., 2014; Hu et al., 2018; Ghazizadeh, 2020; Ding et al., 2021;  
85 Kesserwani and Sharifian, 2023). Aiming to increase computational efficiency by  
86 reducing computing nodes, it adjusts grid size for local grid refinement by domain  
87 features or flow conditions. Yu (2019) used quadtree grids to divide the computational  
88 domain and applied the DBCM to simulate the flooding process. It needs to segment  
89 and merge the grid elements repeatedly during the calculation, which can be time-  
90 consuming and offset the calculation time saved by the optimized grid. Besides, the  
91 mesh generation and flood simulation were compiled in the same code base, which  
92 increased the computational cost and total execution time.

93 Static non-uniform grids have increasingly received attention in recent years,  
94 which simplified grid generation procedure compared with AMR (Caviedes-Voullième  
95 et al., 2012; Hou et al., 2018; Bomers et al., 2019; Ozgen-Xian et al., 2020). Compared  
96 with uniform grids and AMR, it can not only reduce computational nodes, but use  
97 different time steps in different grid sizes to further reduce computation time. Shen et  
98 al. (2021) and Shen and Jiang (2023) divided the computational domain based on static



99 multi-grids, where the different grid size ratios of coarse to fine grids were designed.  
100 But there were two limitations to this scheme. One limitation is that the grids need to  
101 be generated manually, which can be subjective and uncertain. It also needs a heavy  
102 workload, especially for large watersheds. Besides the grid generation, the variable  
103 interpolation between the coarse and fine cells was also not reasonable. There are  
104 shared and hanging nodes at the interpolation interface. Shen et al. (2021) assumed the  
105 variables at the shared nodes were equal to that at the cell center, and the hanging nodes  
106 were obtained from shared nodes. The results showed that this scheme has  
107 unsatisfactory accuracy and frequently fails to converge. Although the multi-grid-based  
108 model can reduce computational time, there are remarkable challenges such as the grid  
109 partition technique, determination of coarse and fine regions, and variables  
110 interpolation between coarse and fine grids.

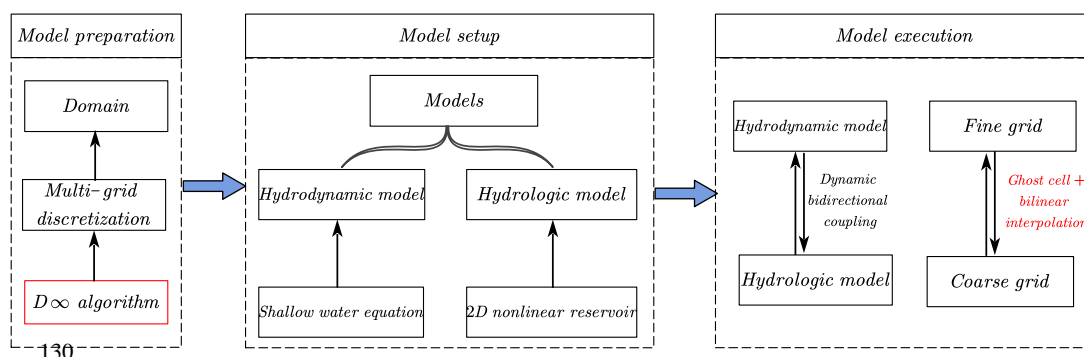
111 The objective of this study is to develop an integrated system that fully couples  
112 the hydrologic and 2D hydrodynamic models, utilize an automated method for efficient  
113 multi-grid mesh generation, and resolve variable interpolation between coarse and fine  
114 grids more accurately. An improved dynamic bidirectional coupling model (IM-DBCM)  
115 was presented, where the 2D nonlinear reservoir (NLR) model was coupled with the  
116 full 2D hydrodynamic model through a CMI. The  $D_\infty$  algorithm was implemented to  
117 divide the computational domain into non-uniform grids automatically. Ghost cells and  
118 bilinear interpolation were used to interpolate variables between the coarse and fine  
119 grids. Three case studies, two laboratory experiments and one real-world watershed,  
120 were conducted, and the simulation results were compared with the original M-DBCM  
121 (OM-DBCM) to evaluate the effectiveness of the improvements.

## 122 **2 Methodology**

123 The Fortran programming language was adopted to apply the coupling model. The



124 framework of IM-DBCM is illustrated in Figure 1. The model consists of two  
 125 components: a hydrologic model (i.e., 2D NLR model) that simulates the runoff  
 126 generation and routing, and 2D hydrodynamic model simulating the flood inundation  
 127 process. Before the model setup, it is required to first design the grids. For the model  
 128 execution, the variables interpolation between coarse and fine grids and the coupling of  
 129 hydrologic and hydrodynamic models are the two main issues that must be addressed.



130

131

Figure 1 Framework of IM-DBCM

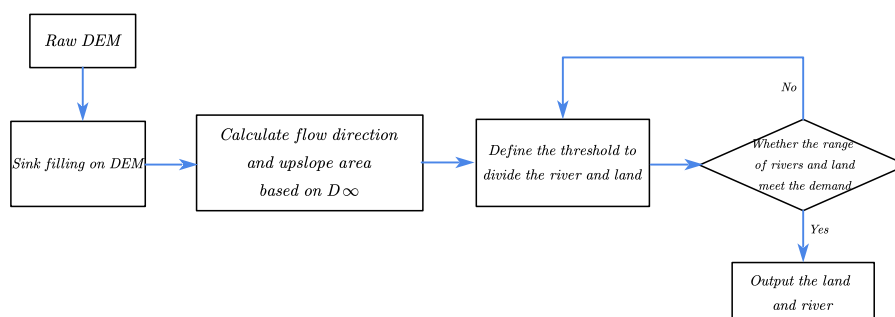
## 132 2.1 Automated multi-grid generation

133 Associated with flood models, the design of computational grids that are scalable  
 134 and suitable for all applications is challenging. The grid generation can be considered  
 135 as a model preprocess, which is the foundation of flood simulation and can influence  
 136 both computational accuracy and efficiency. In this study, a multi-grid generation  
 137 method was proposed based on the  $D_\infty$  algorithm, to generate refined grid cells at flood-  
 138 prone areas where high-resolution representation of topographic features is essential for  
 139 flood simulation while discretizing the rest of the domain using coarse grids. The  $D_\infty$   
 140 algorithm is a method of representing flow directions based on triangular facets in grid  
 141 DEM proposed by Tarboton (1997). It allocates the flow fractionally to each lower  
 142 neighboring grid in proportion to the slope toward that grid. The flow direction is  
 143 determined as the direction of the steepest downward slope on the eight triangular facets



144 formed across a  $3 \times 3$ -pixel window centered on the pixel of interest, which was detailed  
145 by Tarboton (1997). Compared with the D8 algorithm, where the flow is discretized  
146 into only one of eight possible directions, separated by  $45^\circ$ , the  $D_\infty$  algorithm is more  
147 reasonable and accurate for delineating the actual river trend.

148 The process of discretizing computational domain based on the  $D_\infty$  algorithm is  
149 shown in Figure 2. First, a raw DEM was prepared, and sink filling was performed on  
150 the DEM. Second, the  $D_\infty$  algorithm was applied to determine the flow direction on  
151 grids. Subsequently, the upslope area, defined as the total catchment area that is  
152 upstream of a grid center or short length of contour (Moore et al., 1991), was calculated  
153 based on the flow direction. Finally, an area threshold was defined to identify the slope  
154 lands and derive the river drainage networks from accumulated drainage areas. In a grid  
155 cell, if the upslope area was larger than the predefined threshold, it was considered as a  
156 river drainage network; otherwise, it was defined as slope lands. The generated slope  
157 lands and river network were verified through field surveys or satellite images-based  
158 estimates. Generally, the river drainage networks present low slopes and hydraulic  
159 conveyance, which is subject to flooding. Therefore, these areas should be discretized  
160 using fine grids to represent the flooding process in high resolution. However, in the  
161 slope lands, fine grids were not required and coarse grids were used to improve  
162 computational efficiency. Because the regions of interest were of high resolution, the  
163 reliability of the prediction would not deteriorate, although the number of grid cells was  
164 considerably reduced, which can increase model efficiency and capability for flood  
165 simulations over large domains. Compared with manual work, the grid generation  
166 based on the  $D_\infty$  algorithm can both reduce workload and time.



167

168

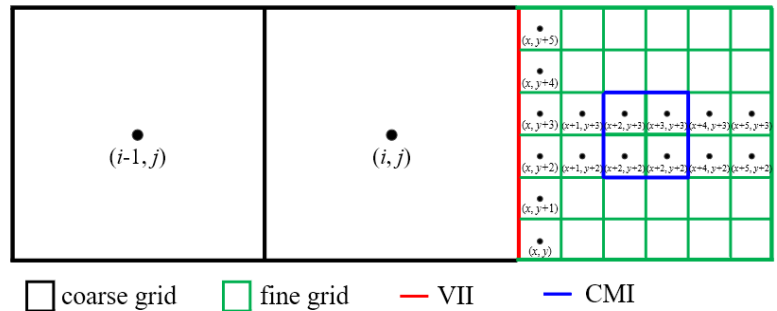
Figure 2 Grid generation based on the  $D_{\infty}$  algorithm

169

A schematic of grid generation is shown in Figure 3. Two types of connecting interfaces are presented, which divide the computing domain into three parts. The first type is the red line (Variable Interpolation Interface, VII) between the coarse and fine grids. The grid cell size changes suddenly on both sides of this line. The second type (Coupling Moving Interface, CMI) is marked in blue on fine grids, which is moving and time-dependent. The first part represents the coarse-grid areas, where the hydrologic model is used to simulate rainfall-runoff. The other two parts are located in the fine-grid areas. The regions between VII and CMI are defined as intermediate transition zones, where the hydrologic model is used to simulate the flooding process. These transition zones facilitate the application of different time steps in different grid cell sizes to improve computational efficiency. The hydrologic and hydrodynamic models are dynamically coupled to represent the flooding process on fine grids, and the CMI is a coupling boundary.

181





182

183 Figure 3. Schematic diagram of grid generation, where  $i$  and  $j$  are the coordinates of  
 184 coarse grid;  $x$  and  $y$  are the coordinates of fine grid; VII is the Variable Interpolation

185 Interface and CMI is the Coupling Moving Interface

186 **2.2 Variable interpolation between coarse and fine grids**

187 During a flow computation, if a cell has a neighbor of different size, interpolation  
 188 may be required to approximate variables in certain locations so that the governing  
 189 equation can be solved smoothly. An example is presented in Figure 4(a), where the  
 190 coarse grid has two eastern neighbors that are half its size. In this case, the variable  
 191 values of the smaller cells are obtained from those of larger cells. In the traditional  
 192 method, these variables are directly calculated using certain interpolation methods.  
 193 There are shared ( $P_1, P_2$ ) and hanging ( $Q$ ) nodes at the interface between the coarse and  
 194 fine grids. In Shen et al. (2021), the variable values on shared nodes can be transmitted  
 195 directly, while the values on hanging nodes were obtained by linear interpolation of the  
 196 shared nodes. This method is simple, feasible and easy to use. However, the variable  
 197 values are stored at the cell center, and there are no values at the interface nodes. Shen  
 198 et al. (2021) assumed that the values at the interface nodes were equal to that at the cell  
 199 center. It is inaccurate to make such an assumption, which can bring errors. And the  
 200 resulting error will increase as the cell size increases.

201 To overcome these drawbacks, ghost cells and bilinear interpolation method were



202 used to interpolate variables between coarse and fine grids. Figure 4(a) shows the  
203 variable interpolation between the coarse and fine grids. Two ghost fine cells were  
204 created, which were overlaid with partial coarse grids. The variables on the ghost fine  
205 cells were interpolated through the coarse and fine grids between the interface, which  
206 were then used as the boundary conditions for the calculation of the fine grids at the  
207 next time step. The bilinear interpolation method was applied. The variable  
208 interpolation may involve variables at locations  $c_1, c_2, c_3, f'_{v1}, f'_{v2}, f_1$  and  $f_2$ . As the  
209 variables are stored at the cell center, the variables at  $c_1, c_2, c_3, f_1$  and  $f_2$  are available  
210 directly. The values at  $f'_{v1}$  and  $f'_{v2}$  are obtained via natural neighbor interpolation, as  
211 follows:

$$212 \quad U_{f'_{v1}} = U_{c_1} + \frac{U_{c_2} - U_{c_1}}{y_{c_2} - y_{c_1}} (y_{f'_{v1}} - y_{c_1}) \quad (1)$$

$$213 \quad U_{f'_{v2}} = U_{c_3} + \frac{U_{c_1} - U_{c_3}}{y_{c_1} - y_{c_3}} (y_{f'_{v2}} - y_{c_3}) \quad (2)$$

214 where  $U_{f'_{v1}}, U_{f'_{v2}}, U_{c_1}, U_{c_2}, U_{c_3}$  are the variables at locations  $f'_{v1}, f'_{v2}, c_1, c_2, c_3$  respectively;  
215  $y_{f'_{v1}}, y_{f'_{v2}}, y_{c_1}, y_{c_2}, y_{c_3}$  are the coordinates in y directions at  $f'_{v1}, f'_{v2}, c_1, c_2, c_3$  respectively.

216 And then, the variables of ghost fine cells at  $f_{v1}$  and  $f_{v2}$  can be calculated based  
217 on that at  $f'_{v1}$  and  $f'_{v2}$ , as follows:

$$218 \quad U_{f_{v1}} = U_{f'_{v1}} + \frac{U_{f_1} - U_{f'_{v1}}}{x_{f_1} - x_{f'_{v1}}} (x_{f_{v1}} - x_{f'_{v1}}) \quad (3)$$

$$219 \quad U_{f_{v2}} = U_{f'_{v2}} + \frac{U_{f_2} - U_{f'_{v2}}}{x_{f_2} - x_{f'_{v2}}} (x_{f_{v2}} - x_{f'_{v2}}) \quad (4)$$

220 where  $U_{f_{v1}}, U_{f_{v2}}$  are the variables of ghost fine cells;  $U_{f_1}, U_{f_2}$  are the variables at  $f_1, f_2$ ,  
221 respectively, which were calculated in the last time step;  $x_{f_1}, x_{f_2}, x_{f_{v1}}, x_{f_{v2}}, x_{f'_{v1}}$  and  $x_{f'_{v2}}$



222 are the coordinates in  $x$  directions at  $f_1, f_2, f_{v1}, f_{v2}, f'_{v1}, f'_{v2}$  respectively.

223 The values at  $f_{v1}, f_{v2}$  were used as the boundary conditions for the calculation of  
224 fine grids.

225 The variable interpolation from fine to coarse grids is presented in Figure 4(b),  
226 where one ghost coarse cell was established. The variables of ghost coarse cells were  
227 determined according to the fine and coarse grids between the interface. The variable  
228 interpolation may involve variables at locations  $c'_v, c_1, f_1, f_2$ . As the variables are stored  
229 at the cell center, the variables at  $c_1, f_1, f_2$  are available directly. The values at  $c'_v$  are  
230 obtained via natural neighbor interpolation, as follows:

$$231 \quad U_{c'_v} = U_{f_2} + \frac{U_{f_1} - U_{f_2}}{y_{f_1} - y_{f_2}} (y_{c'_v} - y_{f_2}) \quad (5)$$

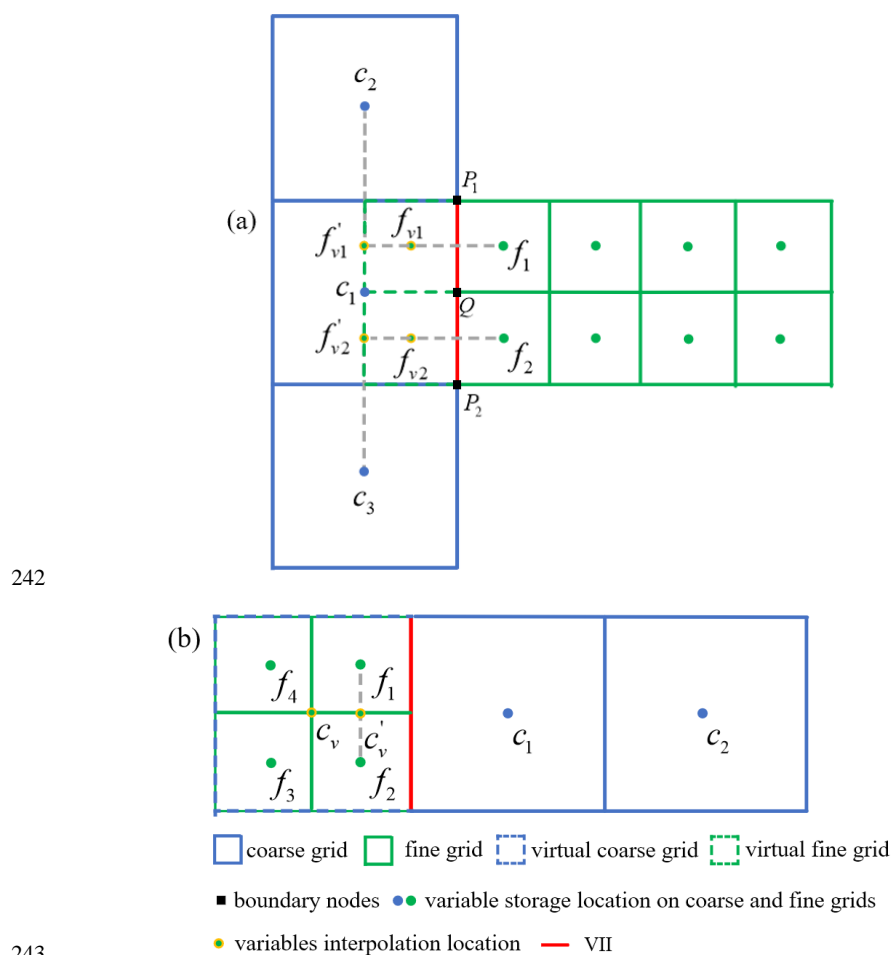
232 where  $U_{c'_v}, U_{f_1}, U_{f_2}$  are the variables at  $c'_v, f_1, f_2$  respectively;  $y_{c'_v}, y_{f_1}, y_{f_2}$  are the  
233 coordinates in  $y$  direction at  $c'_v, f_1, f_2$  respectively.

234 And then, the variables of ghost coarse cells at  $c_v$  can be calculated based on that  
235 at  $c'_v, c_1$ , as follows:

$$236 \quad U_{c_v} = U_{c'_v} + \frac{U_{c_1} - U_{c'_v}}{x_{c_1} - x_{c'_v}} (x_{c_v} - x_{c'_v}) \quad (6)$$

237 where  $U_{c_v}$  are the variables of ghost fine cells;  $U_{c_1}$  are the variables at  $c_1$ , which were  
238 calculated in the last time step;  $x_{c_1}, x_{c'_v}, x_{c_v}$  are the coordinates in  $x$  direction at  $c_1, c'_v, c_v$   
239 respectively.

240 The values at  $c_v$  were used as boundary conditions for the calculation of coarse  
241 grids at the next time step.



242

243

244

245

246

247

248

249

250

251

252

Figure 4. Variables interpolation between coarse and fine grids: (a) from coarse to fine grids and (b) from fine to coarse grids

## 2.3 Numerical models

### 2.3.1 Hydrologic model

In this study, referring to the runoff calculation in the Storm Water Management Model (SWMM), a 2D NLR model, including water balance and Manning equations, was used to simulate rainfall-runoff. In SWMM, the watershed is divided into many water tanks or reservoirs, where 1D NLR model including water balance and 1D Manning equations is used to simulate the runoff (Rossman, 2015). It is a simple and



253 efficient method to calculate the runoff routing. In reality, however, the runoff routing  
254 is a 2D way, so it is not accurate to calculate the 2D runoff routing using 1D NLR model.  
255 Also, it is difficult to directly couple the 1D NLR model with 2D hydrodynamic model.  
256 Therefore, the 2D NLR model was used to simulate the 2D surface runoff routing in  
257 this study, as shown in Eqs. (7-11).

$$258 \quad \frac{V_i^{n+1} - V_i^n}{\Delta t} = (Q_x)_{in\ i} - (Q_x)_{out\ i} + (Q_y)_{in\ i} - (Q_y)_{out\ i} + A_i q_r^n \quad (7)$$

$$259 \quad (Q_x)_{in\ i} - (Q_x)_{out\ i} = -\sum_{l=1}^L (q_{x\ \Gamma}^n \cdot n_x)_l \Delta L_l \quad (8)$$

$$260 \quad (Q_y)_{in\ i} - (Q_y)_{out\ i} = -\sum_{l=1}^L (q_{y\ \Gamma}^n \cdot n_y)_l \Delta L_l \quad (9)$$

$$261 \quad q_x = \frac{h^{5/3} S_x^{1/2}}{n_r} \quad (10)$$

$$262 \quad q_y = \frac{h^{5/3} S_y^{1/2}}{n_r} \quad (11)$$

263 where the superscript  $n$  and  $n+1$  is the time step;  $V$  is the water volume of grid ( $m^3$ );  
264  $(Q_x)_{in\ i}, (Q_x)_{out\ i}$  is the inflow and outflow of grid  $i$  in  $x$  direction ( $m^3/s$ );  
265  $(Q_y)_{in\ i}, (Q_y)_{out\ i}$  is the inflow and outflow of grid  $i$  in  $y$  direction ( $m^3/s$ );  $q_r$  indicates  
266 runoff rate of grid  $i$  (mm/h), which is rainfall intensity minus infiltration rate;  $A_i$  is the  
267 area of grid  $i$  ( $m^2$ );  $q_x, q_y$  are the unit discharge stored at cell-center along  $x$  and  $y$   
268 direction ( $m^2/s$ ), with  $h, u$  and  $v$  being water depth (m), flow velocity (m/s) in  $x$  and  $y$   
269 directions, respectively;  $q_{x\ \Gamma}, q_{y\ \Gamma}$  are the unit discharge at grid boundary in  $x$  and  $y$   
270 direction, respectively ( $m^2/s$ ), which are calculated based on  $q_x, q_y$ ;  $\Delta L_l$  is the side  
271 length of grid (m);  $l = 1, 2, 3, \dots, L$  is the number of edges of cell;  $n_r$  is the Manning  
272 roughness coefficient;  $S_x$  and  $S_y$  are water level gradients along  $x$  and  $y$  direction,



273 respectively,  $S_x = -\frac{\partial}{\partial x}(z_b + h)$ ,  $S_y = -\frac{\partial}{\partial y}(z_b + h)$ , where  $z_b$  is the surface elevation.

### 274 **2.3.2 Hydrodynamic model**

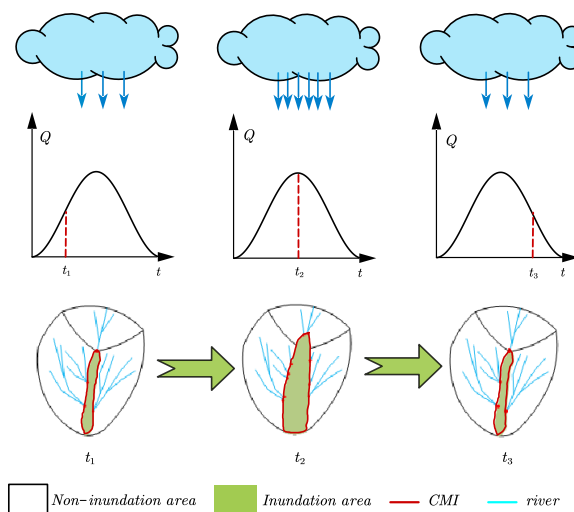
275 The 2D shallow water equations (SWEs), consisting of mass and momentum  
276 conservation equations (Toro 2001), were used to represent the hydrodynamic model.  
277 The Godunov-type finite volume scheme with a Harten-Lax-van Leer contact (HLLC)  
278 approximate Riemann solver (Toro et al., 1994) was adopted to solve the 2D SWEs,  
279 and the second-order accuracy in temporal and spatial discretization was obtained based  
280 on the Runge-Kutta method and Monotone Upstream-centered Schemes for  
281 Conservation Laws (MUSCL) (Van Leer, 1979). The solution of SWEs was detailed in  
282 many references (Toro 2001; Jiang et al., 2021).

### 283 **2.4 Dynamic bidirectional coupling of hydrologic and hydrodynamic models**

284 The hydrologic and hydrodynamic models were coupled dynamically and bi-  
285 directionally. A water depth threshold was defined in advance and used to determine  
286 the state of the cell. In a grid cell, if the water depth was lower than the predefined  
287 threshold, it was defined as a non-inundation region where the hydrologic model was  
288 applied. Conversely, if the water depth was higher than the threshold, it was considered  
289 an inundation region where the 2D hydrodynamic model was applied. When the rainfall  
290 intensity increased, the water depth increased because of the gradual accumulation of  
291 surface water volume. Once the water depth exceeds the predefined threshold, the non-  
292 inundation regions defined last time step may change to the inundation regions. The  
293 inflow discharge positions, flow path, and discharge values subsequently changed, as  
294 shown in Figure 5. Therefore, a CMI was formed between the inundation and non-  
295 inundation regions. The hydrologic and 2D hydrodynamic models were coupled bi-  
296 directionally, and the coupling interface was moving and time-dependent. The key issue  
297 with the coupled model was to establish a reasonable approach for determining the



298 fluxes passing through the coupling interface, which should integrate the effect of the  
 299 current flow state obtained from these two models on both sides of the coupling  
 300 interface. The coupling method was described by Jiang et al. (2021).



301

302 Figure 5. Variation in non-inundation and inundation regions with changing rainfall  
 303 conditions

### 304 2.5 Time step

305 An explicit scheme was used to solve the hydrologic and hydrodynamic models  
 306 over time. The time step was constrained by the Courant-Friedrichs-Lewy condition  
 307 (Delis and Nikolos, 2013), where the time step was a dynamic adjustment based on the  
 308 velocity and water depth in the computational domain. Different time steps were  
 309 adopted for the coarse and fine grids, and the time step of the fine grids was determined  
 310 as follows:

$$311 \quad \Delta t_f = C \cdot \min \left( \frac{\min(\Delta x_f)}{\max(|u_f| + \sqrt{gh_f})}, \frac{\min(\Delta y_f)}{\max(|v_f| + \sqrt{gh_f})} \right) \quad (12)$$

312 where  $\Delta t_f$  is the time step of fine grids;  $C$  is a constant used to maintain format stability;



313  $\Delta x_f$  and  $\Delta y_f$  are the side lengths of fine grid in  $x$  and  $y$  directions;  $u_f$  and  $v_f$  are the  
314 flow velocities on fine grids along  $x$  and  $y$  directions, respectively;  $h_f$  is the water depth  
315 on fine grids.

316 The time step of the coarse grids ( $\Delta t_c$ ) was determined based on that of the fine  
317 grids. If the size of the coarse grid was  $k$  times that of the fine grid, the time step of the  
318 coarse grid was determined to be  $\Delta t_c = k\Delta t_f$ .

### 319 **3 Results**

320 The performance of the IM-DBCM was analyzed by applying it to two 2D rainfall-  
321 runoff experiments and one real-world flooding process. And the OM-DBCM  
322 developed by Shen et al. (2021) was applied to the same cases for comparison with the  
323 IM-DBCM.

#### 324 **3.1 Rainfall over a plane with varying slope and roughness**

325 In this case, a sloping plan measuring  $500m \times 400m$  was designed, with slopes  
326  $S_{ox} = 0.02 + 0.0000149x$  and  $S_{oy} = 0.05 + 0.0000116y$  along the  $x$  and  $y$  directions,  
327 respectively (Jaber and Mohtar, 2003). The Manning coefficient is equal to  
328  $n = \sqrt{n_x^2 + n_y^2}$ , where  $n_x = 0.1 - 0.0000168x$  and  $n_y = 0.1 - 0.0000168y$ . The rainfall  
329 intensity is given by a symmetric triangular hyetograph  $r = r(t)$ , with  
330  $r(0) = r(200\text{min}) = 0$  and  $r(100\text{min}) = 0.8 \times 10^{-5} m/s$ . The total simulation time was  
331 14,400 s.

332 Different cases with various grid resolutions were developed to divide the  
333 computational domain based on the  $D_\infty$  algorithm, as listed in Table 1. In these cases,  
334 the size of all the fine grids was  $1m \times 1m$ . The grid discretization of different cases is  
335 shown in Figure S1 in Supplement.

336 Table 1 Different cases designed to simulate





Cases	The ratio of coarse to fine grids	Number of grids
case12	1:2	112,100
case15	1:5	86,840
case10	1:10	83,220

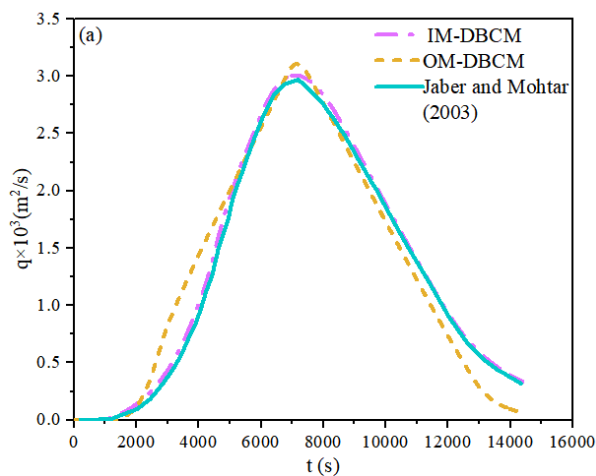
337 The hydrographs at the outlet node of coordinates of (500m, 400m) obtained from  
338 different models were shown in Figure 6. A model proposed by Jaber and Mohtar (2003)  
339 was also used to simulate the overland runoff. Because very fine grids and small time  
340 step were used to divide the computational domain to obtain more accurate results in  
341 the model developed by Jaber and Mohtar (2003), the results calculated by Jaber and  
342 Mohtar (2003) can be used as a reference solution.

343 From Figure 6, the IM-DBCM held a shape close to the results simulated by Jaber  
344 and Mohtar (2003) in all cases, as well as the peak discharge. But the peak discharge  
345 of the hydrograph is slightly overestimated by the OM-DBCM, which may be attributed  
346 to the difference in the variable interpolation between the coarse and fine grids. In the  
347 OM-DBCM, variables at the interpolation interface were equal to that at the cell center,  
348 which was then used to interpolate variables between the coarse and fine grids through  
349 shared and hanging nodes. This interpolation method had two drawbacks. Firstly, it is  
350 not reasonable to assume the variables at the interpolation interface are equal to that at  
351 the cell center, and the resulting error could increase as the grid size increases. Besides,  
352 compared with bilinear interpolation, the values at the hanging nodes are calculated by  
353 linear interpolation through shared nodes, which may result in relatively large errors.  
354 The results show that the methods to interpolate variable between the coarse and fine  
355 grids by developing ghost cells proposed in this study has acceptable accuracy.

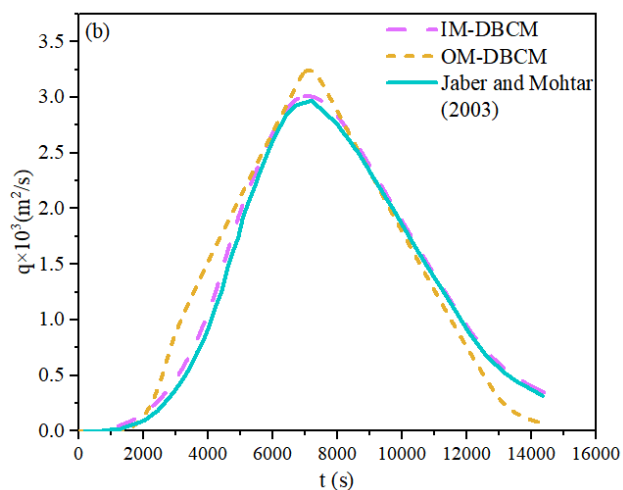
356 To quantitatively assess the performance of IM-DBCM, the Root Mean Square  
357 Error (RMSE) of different cases was computed. The RMSEs of case12, case15 and  
358 case10 were 4.01E-04, 7.85E-03 and 3.25E-02, respectively. It is shown that the error



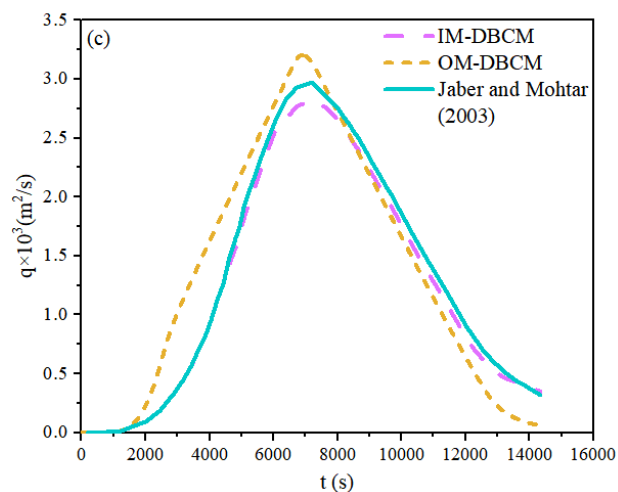
359 gradually increased with the increasing of the ratio of coarse to fine grids. The IM-  
360 DBCM may capture the shape of the hydrograph in case12 and case15, both in limbs  
361 and peak discharge, but the peak discharge is slightly underestimated in case10. A  
362 possible explanation is that, compared to the coarse grids, the fine grids could better  
363 capture the geometry of the channel cross-sections. High-resolution grids can better  
364 represent small-scale topographic features and flow passages (Hou et al., 2018);  
365 consequently, the simulation results on case12 and case15 are more satisfactory than  
366 those on case10. Similarly, the simulation accuracy of the OM-DBCM also gradually  
367 decreased with the increasing of the ratio of coarse to fine grids. Overall, the benefit of  
368 using the IM-DBCM for the flood simulations is evident.



369



370



371

372 Figure 6 Hydrographs obtained from different models: (a) case12, (b) case15 and (c)

373

case10

### 374 3.2 2D rainfall-runoff experiment

375 In this case, the IM-DBC was used to compute the hydrograph generated by

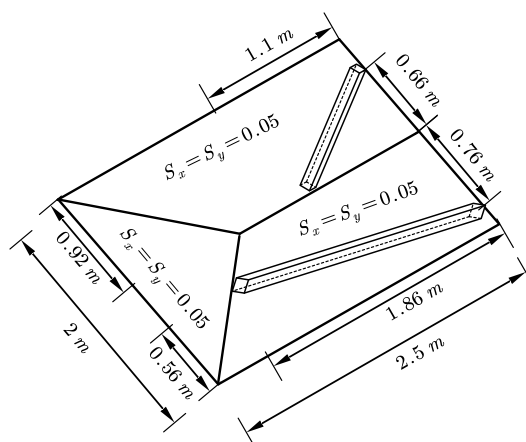
376 uniform rainfall conditions over a simple 2D geometry. The numerical results were

377 compared with experimental data obtained in a laboratory model developed by Cea et

378 al. (2008). The 2D geometry used in the experiment comprised a rectangular basin



379 composed of three stainless-steel planes, each with a slope of 0.05. The basin had two  
380 walls that increased the residence time of the runoff in the basin and the length of the  
381 outlet hydrograph. The geometric dimensions of the basin are shown in Figure 7.



382

383 Figure 7. Geometry and size of the 2D basin for the rainfall-runoff experiment

384 Two rainfall intensities were simulated. In case01, the rainfall intensity was 317  
385 mm/h for 45 s. In case02, the rainfall had an intensity of 320 mm/h for 25 s, then it  
386 stopped for 7 s and started again continuing for 25 s with an intensity of 328 mm/h.

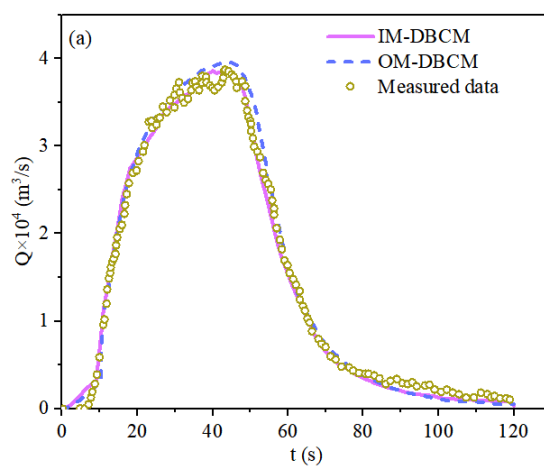
387 The computational basin was divided into coarse and fine grids based on the  $D_{\infty}$   
388 algorithm. The size of the fine grids was  $0.01\text{m} \times 0.01\text{m}$ , whereas that of the coarse  
389 grids was  $0.02\text{m} \times 0.02\text{m}$ . The grid partition is presented in Figure S2 in Supplement.  
390 According to Cea et al. (2008), the Manning coefficient was  $0.009\text{ s/m}^{1/3}$ .

391 Figure 8 shows a comparison between the numerical and experimental outlet  
392 hydrographs. The shape of hydrographs was well predicted in both cases, indicating  
393 that the IM-DBCM could capture the flow process and exhibited satisfactory accuracy.  
394 In case02, the first peak discharge rate occurred when the rainfall stopped for the first  
395 time. Subsequently, the discharge rate began to decrease. After 7 s, rainfall started again,  
396 and the discharge rate continued to decrease. The RMSEs of discharge simulated by

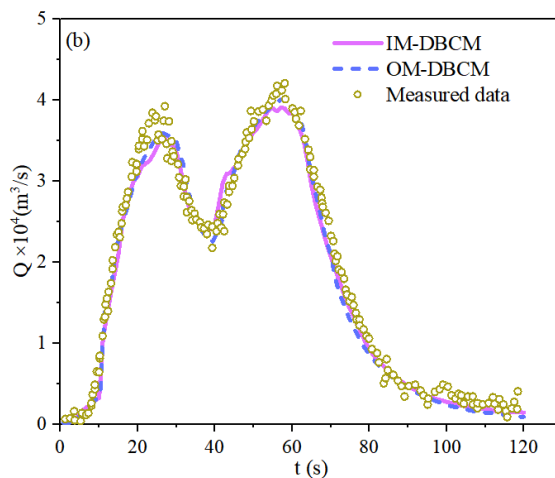


397 IM-DBCM in case01 and case02 were 0.107 and 0.023 respectively. The numerical  
398 results were in good agreement with the experimental data. Compared to the results  
399 obtained from OM-DBCM, the simulation results obtained from IM-DBCM were  
400 closer to the experimental data. The results for case01 were slightly over-predicted by  
401 the OM-DBCM.

402



403



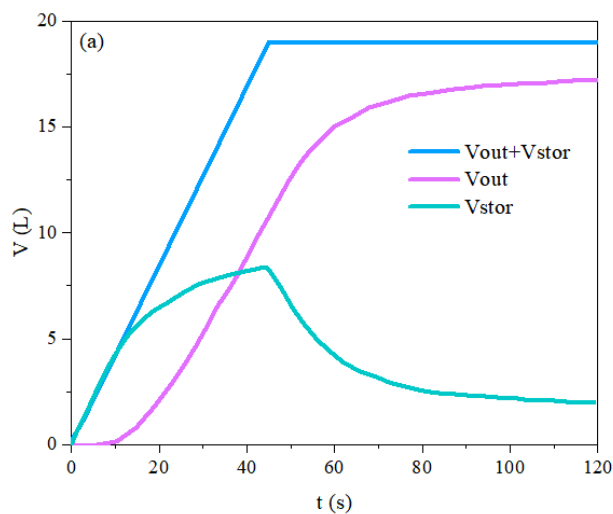
404 Figure 8. Simulated and measured discharge rate at different cases: (a) case01 and (b)

405 case02

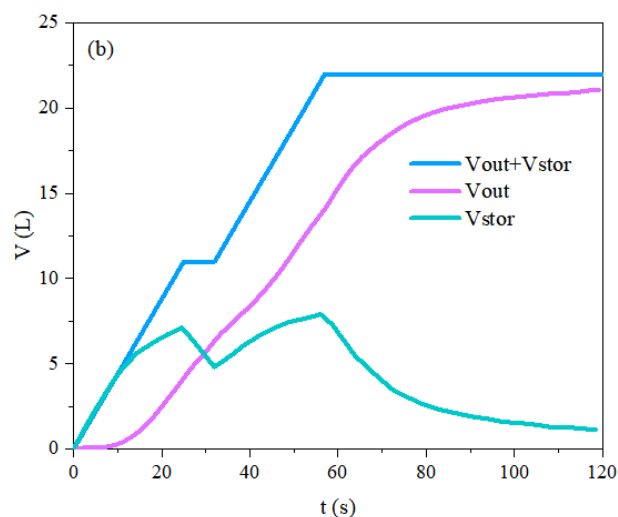
406 To verify the conservation of the IM-DBCM, the inflow and outflow of different



407 cases in this basin were determined to represent the water balance, as shown in Figure  
408 9. In case01, the outflow increased with the increasing of simulation time, whereas the  
409 water storage increased first and then decreased. When the rainfall stopped at 45 s,  
410 water was discharged from the basin; therefore, the water storage decreased. The sum  
411 of the outflow and storage was equal to the accumulated rainfall, indicating that the IM-  
412 DBCM can ensure the conservation of water mass. In case02, the outflow continuously  
413 increased. Two peak flows were observed for the water storage, which was caused by  
414 the intermittent rainfall. Overall, the sum of the outflow and water storage was equal to  
415 the accumulated rainfall, indicating that the IM-DBCM ensured mass conservation.



416



417

418 Figure 9. Inflow and outflow for different cases: (a) case01 and (b) case02, where  
419 “Vout” refers to the outflow and “Vstor” refers to water storage in the computational  
420 basin

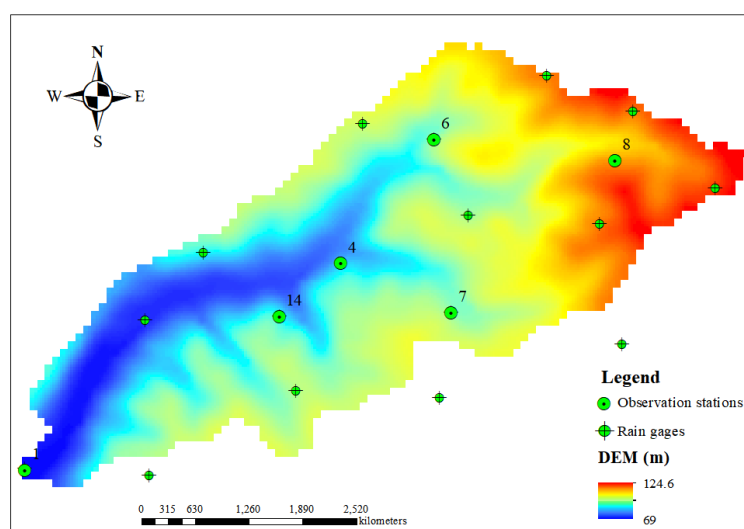
### 421 3.2 Flood simulation in a natural watershed

422 The Goodwin Creek watershed, located in Panola County, Mississippi, USA, is  
423 often selected as a benchmark to assess the capability of flood models because of  
424 sufficient available observed data. Drainage is westerly to Long Creek which flows into  
425 the Yocona River, one of the main rivers of the Yazoo River, a tributary of the  
426 Mississippi River. The Goodwin Creek watershed covers an area of 21.3 km<sup>2</sup>. The  
427 overall terrain gradually decreased from northeast to southwest, which is consistent  
428 with the trend of the main channel, and the elevation ranged from 71 to 128 m. The  
429 computational basin and bed elevations are shown in Figure 10.

430 Land use in this watershed was divided into four classes including forest, water,  
431 cultivated, and pasture, and their Manning coefficients were 0.05, 0.01, 0.03, and 0.04,  
432 respectively (Sánchez, 2002). The infiltration coefficients of different soil types were  
433 determined according to Blackmarr (1995). The rainfall event in sixteen rain gages (see



434 Figure 10) of October 17, 1981 was chosen for simulation (Sánchez, 2002), and the  
435 inverse distance interpolation method (Barbulescu, 2016) was used to calculate the  
436 precipitation over the entire watershed. The rainfall duration was 4.8 h. Rainfall was  
437 spatially distributed at different times, as shown in Figure S3 in Supplement. There  
438 were measured data in six observation stations (i.e., 1, 4, 6, 7, 8 and 14) Blackmarr  
439 (1995), whose locations were shown in Table S1 in Supplement, and the simulated  
440 results were compared with the measured data in these stations.



441

442

Figure 10. Overview of the Goodwin Creek watershed

443

444

445

446

447

448

The simulations were performed for 12 h. Different cases with various grid resolutions were developed to verify the computational efficiency and numerical accuracy of IM-DBCM, as listed in Table 2. In M-DBCM, the rivers were covered by fine-grid cells with dimensions of 10 m × 10 m, whereas the coarseness in the rest of the domain was increased to higher levels, as presented in Figure S4 in Supplement.

Table 2. Different cases designed to simulate the Goodwin Creek watershed

Cases	The ratio of coarse to fine grids	Number of grids
case12	1:2	104,555





case15	1:5	65,240
case10	1:10	59,431

449 The OM-DBCM was also used to simulate the rainfall runoff with the same  
 450 resolutions. The Nash-Sutcliffe efficiency (NSE) was used to quantify errors in each  
 451 model. NSE ranges between  $-\infty$  and 1.0, with NSE=1 being the optimal value. The  
 452 NSEs of IM-DBCM and OM-DBCM were shown in Table 3. From this table, the NSEs  
 453 of IM-DBCM were higher than that of OM-DBCM at most stations, which was  
 454 probably caused by the different interpolation method at the interface between coarse  
 455 and fine grids. It is verified that the IM-DBCM has relatively high accuracy in  
 456 simulating rainfall-runoff. In OM-DBCM, it is unreasonable to make the variables at  
 457 the interface between coarse and fine grids equal to that at the cell center, which can  
 458 bring errors. The induced error will increase as the ratio of coarse and fine grids increase.  
 459 Therefore, it is also observed that the NSEs of OM-DBCM decreased with the increased  
 460 ratio of coarse and fine grids. It is indicated that the ghost cells and bilinear interpolation  
 461 used in the IM-DBCM to interpolate variables between coarse and fine grids can make  
 462 the simulation more reasonable.

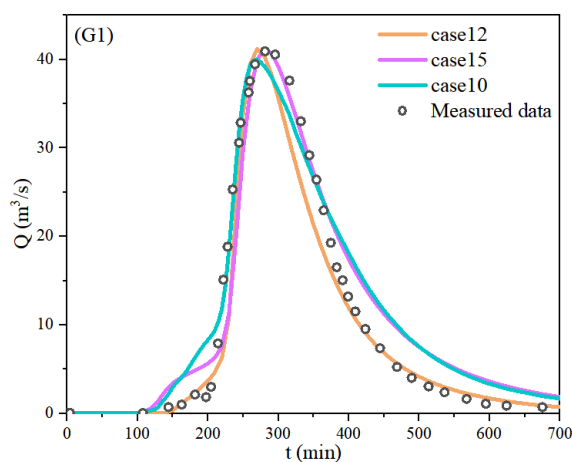
463 Table 3 NSEs of different models (“IM” and “OM” refer to IM-DBCM and OM-  
 464 DBCM, respectively)

Station	G1		G4		G6		G7		G8		G14	
	IM	OM	IM	OM	IM	OM	IM	OM	IM	OM	IM	OM
case12	0.9496	0.9108	0.9611	0.9011	0.9904	0.8982	0.9658	0.9004	0.9435	0.9104	0.9311	0.8804
case15	0.9399	0.8766	0.9404	0.8800	0.9426	0.8819	0.9258	0.8931	0.9341	0.8942	0.9001	0.7942
case10	0.9207	0.8261	0.8907	0.8435	0.9513	0.7977	0.9358	0.8525	0.9358	0.8678	0.9135	0.8078



465 Figure 11 shows a comparison of the measured and simulated hydrographs by IM-  
466 DBCM at the monitoring gauges, whose locations are presented in Figure 10. At all  
467 gauges, the hydrographs obtained from different cases were well aligned with the  
468 measured data, which indicates that the IM-DBCM could reliably reproduce the flood  
469 wave propagation in the complex topography. The results of case12, in general, were  
470 better than those of case15 and case10, especially at station G1. A possible explanation  
471 is that a finer grid is needed to better capture the watershed geometry and obtain more  
472 satisfactory simulation accuracy. The cell size of case15 and case10 is larger than that  
473 of case12.

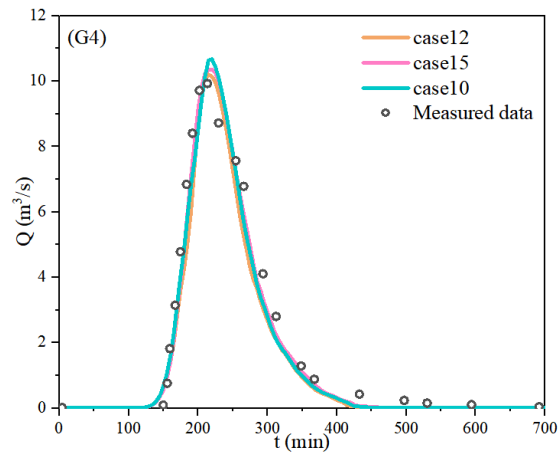
474 Compared with other stations, at station G1, the simulation results obtained from  
475 case15 and case10 deviated substantially from the measured data, especially at receding  
476 limb of the hydrographs. We deduced that the reason for this discrepancy is not the  
477 mesh partitioning, but the location of the G1. G1 is located at the watershed outlet,  
478 where water flows out of the watershed from here. The errors generated upstream may  
479 be accumulated at this station. Despite the deviation, the overall trend of the  
480 hydrographs indicated that the IM-DBCM is satisfactory and can reliably reproduce  
481 flood wave propagation in complex topography.



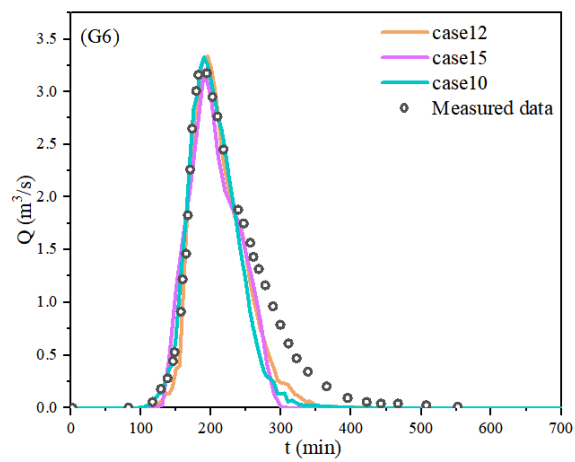
482



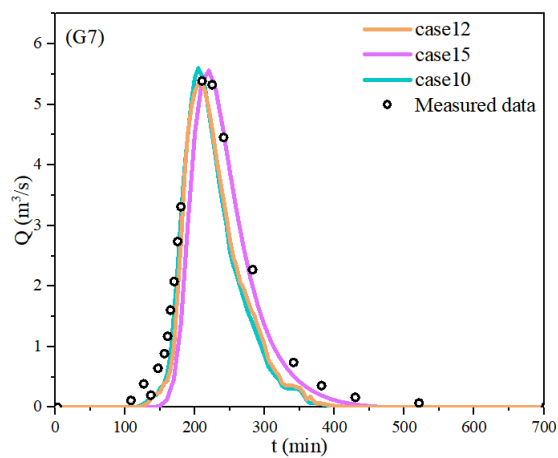
483

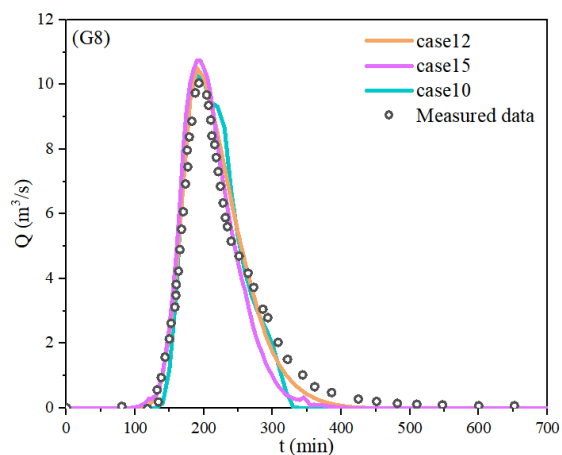


484

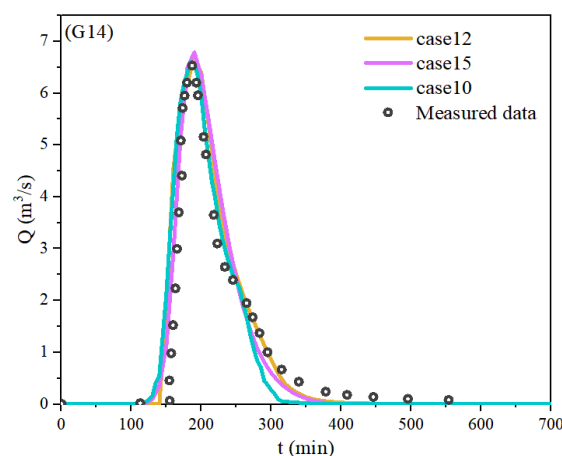


485





486



487

488

Figure 11. Hydrographs obtained from different cases

489

490

491

492

493

494

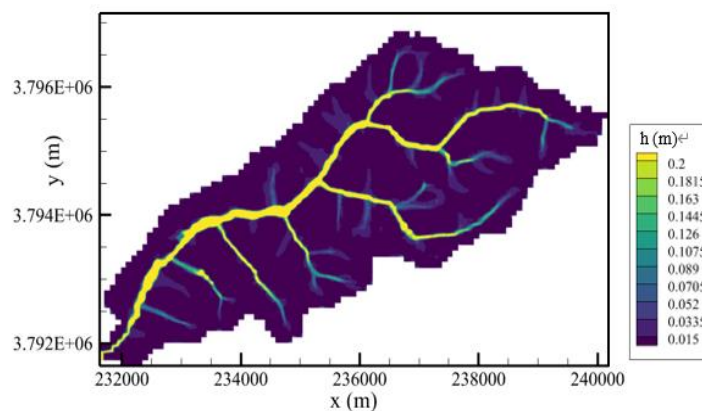
495

496

The water depth and location of the coupling interface at different times are shown in Figure 12. The position of the coupling interface was time-dependent. From 0 to 5 h, the water depth in the computational basin increased with the rainfall. Once the water depth was higher than the predefined threshold, the regions were defined as inundation regions and the hydrodynamic model was used to simulate the rainfall runoff. The water depth peaked in the watershed at 5 h, as shown in Figure 12(a1), and most of the regions were defined as inundation regions, as shown in Figure 12(a2). After 5 h, when rainfall stopped, the water depth in the computational basin decreased (Figure 12(b1)). When



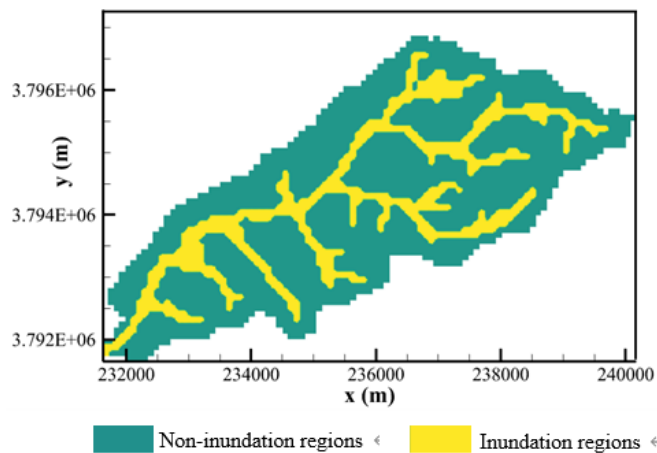
497 the water depth was lower than the predefined threshold, the inundation regions defined  
498 last moment became non-inundation regions. Accordingly, as shown in Figure 12(b2),  
499 the non-inundation regions expanded, whereas the inundation regions decreased. The  
500 location of the coupling interface was shifted to the inundation regions defined at the  
501 last moment. The results indicated that the coupling interface shifted during the  
502 simulation, which was consistent with the flood migration process.



503

504

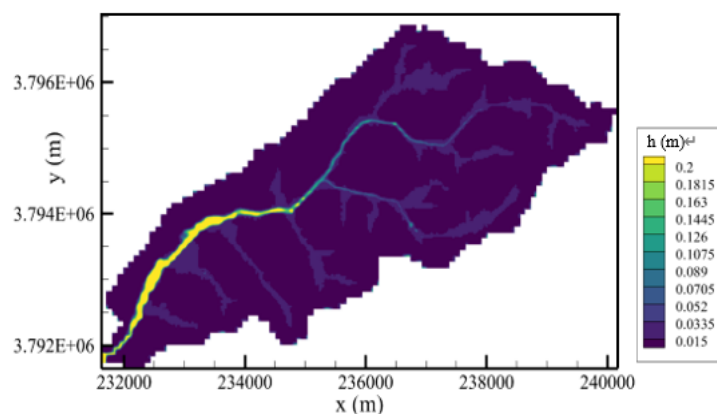
(a1) Water depth at  $t = 5$  h



505

506

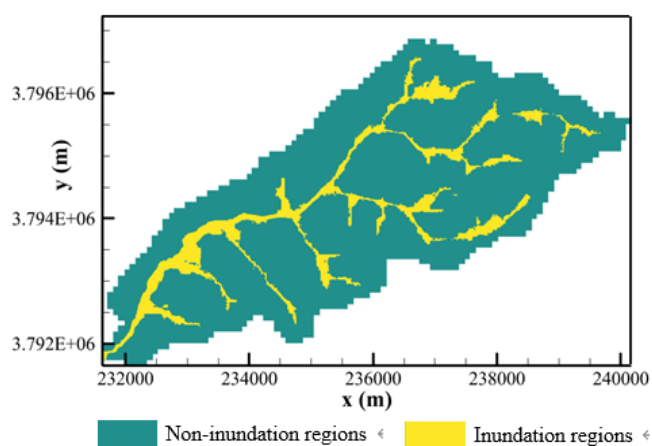
(a2) Position of the coupling interface at  $t = 5$  h



507

508

(b1) Water depth at  $t = 8$  h



509

510

(b2) Position of the coupling interface  $t = 8$  h

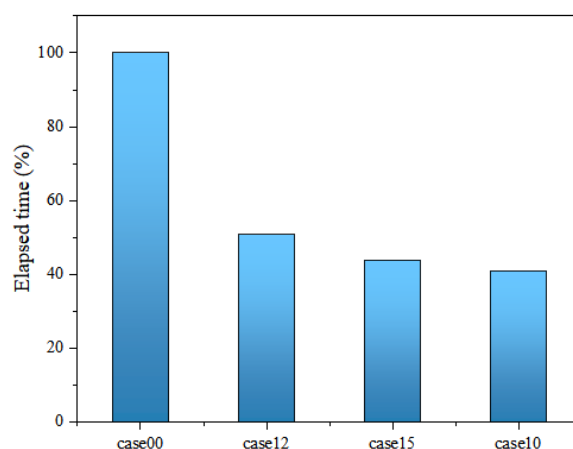
511 Figure 12. Water depth and position of the coupling interface of the hydrologic-

512 hydrodynamic model at different times

513 In terms of efficiency, the total execution time of IM-DBCM was compared with  
514 the uniform grid-based model (case00), as shown in Figure 13. The total execution time  
515 of the different cases ranked from highest to lowest is as follows: case00 > case12 >  
516 case15 > case10. Uniform fine grids were used to divide the computing zones in case00,  
517 and 207,198 computational grids were generated. Compared with case00, most of the  
518 areas were discretized with coarse grids, and only a small part of the regions was



519 calculated based on fine grids in IM-DBCM; the computational grids of the multi-grid-  
520 based model (Table 2) were considerably lower than that of case00. Furthermore,  
521 case12 required less computational time than case15 and case10. The size of the fine  
522 grid cell was the same (10 m × 10 m) in case12, case15 and case10. However, the size  
523 of the coarse grid cell was twice that of the fine grids in case02, whereas the size of  
524 coarse grid cell was five or ten times that of fine grids in case 15 or case10. Therefore,  
525 fewer computational grid points were presented in case15 and case10, which required  
526 less time for calculation, and the computational efficiency could be further improved.  
527 This indicates that the computational time decreases when the size ratio of the coarse  
528 grid to the fine grid increases. Thus, the advantages of using IM-DBCM based on multi-  
529 grids for large-scale flood simulations are evident. The difference in total runtime  
530 between the IM-DBCM and OM-DBCM is the time spent on grid partitioning. In the  
531 OM-DBCM, the computational domain is divided manually, which is highly subjective,  
532 and the computational time varied from person to person.



533

534 Figure 13 The relative difference in computation time of different cases

534

#### 535 4 Conclusions

536 An improved dynamic bidirectional coupled hydrologic-hydrodynamic model



537 based on multi-grid (IM-DBCM) was presented in this study. A multi-grid system was  
538 generated based on the  $D_{\infty}$  algorithm, dividing regions that required high-resolution  
539 representation using fine grids and the rest using coarse grids to reduce computational  
540 load. A two-dimensional non-linear reservoir was adopted in the hydrologic model,  
541 while two-dimensional shallow water equations were applied in the hydrodynamic  
542 model. The hydrologic model was applied to the coarse-grid regions, whereas the  
543 hydrologic and hydrodynamic models were coupled in a bidirectional manner for the  
544 fine-grid areas. Different time steps were adopted in coarse and fine grids. Ghost cells  
545 and bilinear interpolation were used to interpolate variables between coarse and fine  
546 grids. The hydrologic and hydrodynamic models were dynamically and bidirectionally  
547 coupled with a time-dependent and moving coupling interface.

548 The performance of IM-DBCM was verified using three cases. The IM-DBCM  
549 was demonstrated to effectively simulate flow processes and ensure reliable simulation.  
550 Compared with the OM-DBCM, the results obtained from the IM-DBCM were well  
551 aligned with the measured data, and it could reliably reproduce the flood wave  
552 propagation in complex topography. In addition to producing numerical results with  
553 similar accuracy, the IM-DBCM saved computational time compared with the model  
554 on fine grids. Furthermore, a moving coupling interface between the hydrologic and  
555 hydrodynamic models was observed in the IM-DBCM. The IM-DBCM has both high  
556 computational efficiency and numerical accuracy, which was adapted adequately to the  
557 real-life flooding process and provided practical and reliable solutions for rapid flood  
558 prediction and management, especially in large watersheds.

559 The IM-DBCM accurately and efficiently reproduces the flooding process and has  
560 the potential for a wide range of practical applications. Adding a one-way  
561 hydrodynamic model to the model could further enhance its performance. A one-way





562 model can simulate flow in a narrow river, saving more time than using a two-way  
563 hydrodynamic model.

#### 564 **Data availability**

565 Model simulation and calibration data are available upon request from the  
566 corresponding author. Digital elevation model data are provided by the Geospatial Data  
567 Cloud at <http://www.gscloud.cn>. The data sets of Soil Properties and Land cover are  
568 provided by Sánchez (2002) and Blackmarr (1995). The rainfall and measured data  
569 were Blackmarr (1995).

#### 570 **Author contributions**

571 Yanxia Shen designed the methodology and carried out the investigation. Qi Zhou  
572 provided the original model input data. The study was supervised by Chunbo Jiang.  
573 Yanxia Shen prepared the first draft of the manuscript and Zhenduo Zhu revised and  
574 improved the original manuscript.

#### 575 **Competing interests**

576 The authors declare that they have no conflict of interest.

#### 577 **Acknowledgements**

578 This study was supported by the National Natural Science Foundation of China  
579 (Grant No. 52179068) and the Key Laboratory of Hydrosience and Engineering (Grant  
580 No. 2021-KY-04). The authors thank the anonymous reviewers for their valuable  
581 comments.

#### 582 **References**

583 Barbulescu, A.: A new method for estimation the regional precipitation. Water  
584 Resources Management, 30(1), 33-42, 2016. [https://doi.org/10.1007/s11269-015-](https://doi.org/10.1007/s11269-015-1152-2)  
585 [1152-2](https://doi.org/10.1007/s11269-015-1152-2)  
586 Bates, P.D.: Flood inundation prediction. Annual Review of Fluid Mechanics, 54:287-



- 587 315, 2022. <https://doi.org/10.1146/annurev-fluid-030121-113138>
- 588 Bholá, P.K., Leandro, J., Disse, M.: Framework for offline flood inundation forecasts  
589 for two-dimensional hydrodynamic models. *Geosciences (Switzerland)*, 8(9), 346,  
590 2018. <https://doi.org/10.3390/geosciences8090346>
- 591 Blackmarr, W.: Documentation of hydrologic, geomorphic, and sediment transport  
592 measurements on the Goodwin Creek experimental watershed, northern  
593 Mississippi, for the period 1982-1993. Technical Report for United States  
594 Department of Agriculture: Oxford, MS, USA, October, 1995.
- 595 Bomers, A., Schielen, R.M.J., Hulscher, S.J.M.H.: The influence of grid shape and grid  
596 size on hydraulic river modelling performance. *Environmental Fluid Mechanics*.  
597 19(5), 1273-1294, 2019. <https://doi.org/10.1007/s10652-019-09670-4>
- 598 Buttinger-Kreuzhuber, A., Konev, A., Horvath, Z., Cornel, D., Schwerdorf, I., Bloeschl,  
599 G., Waser, J.: An integrated GPU-accelerated modeling framework for high-  
600 resolution simulations of rural and urban flash floods. *Environmental Modelling*  
601 & Software, 156,105480, 2022. <https://doi.org/10.1016/j.envsoft.2022.105480>
- 602 Cea, L., Puertas, J., Pena, L., Garrido, M.: Hydrologic forecasting of fast flood events  
603 in small catchments with a 2D-SWE model, Numerical model and experiment  
604 validation. World Water Congress, 1-4, Montpellier, France, 2008.
- 605 Caviedes-Voullième, D., García-Navarro, P., Murillo, J.: Influence of mesh structure  
606 on 2D full shallow water equations and SCS curve number simulation of  
607 rainfall/runoff events. *Journal of Hydrology*, 448-449(2), 39-59, 2012.  
608 <https://doi.org/10.1016/j.jhydrol.2012.04.006>
- 609 Choi, C.C., Mantilla, R.: Development and Analysis of GIS Tools for the Automatic  
610 Implementation of 1D Hydraulic Models Coupled with Distributed Hydrological  
611 Models. *Journal of Hydrologic Engineering*, 20, 06015005, 2015.



- 612 [https://doi.org/10.1061/\(ASCE\)HE.1943-5584.0001202](https://doi.org/10.1061/(ASCE)HE.1943-5584.0001202)
- 613 Costabile, P., Costanzo, C.: A 2D-SWEs framework for efficient catchment-scale  
614 simulations: hydrodynamic scaling properties of river networks and implications  
615 for non-uniform grids generation. *Journal of Hydrology*, 599(6402), 126306, 2021.  
616 <https://doi.org/10.1016/j.jhydrol.2021.126306>
- 617 Delis, A., Nikolos, I.: A novel multidimensional solution reconstruction and edge-based  
618 limiting procedure for unstructured cell-centered finite volumes with application  
619 to shallow water dynamics. *International Journal for Numerical Methods in Fluids*,  
620 71: 584-633, 2013. <https://doi.org/10.1002/flid.3674>
- 621 Donat, R., Marti M.C., Martinez-Gavara, A., Mulet P.: Well-balanced adaptive mesh  
622 refinement for shallow water flows. *Journal of Computational Physics*, 257:937-  
623 53, 2014. <https://doi.org/10.1016/j.jcp.2013.09.032>
- 624 Ding, Z.L., Zhu, J.R., Chen, B.R., Bao, D.Y.: A Two-Way Nesting Unstructured  
625 Quadrilateral Grid, Finite-Differencing, Estuarine and Coastal Ocean Model with  
626 High-Order Interpolation Schemes. *Journal of Marine Science and Engineering*,  
627 9(3), 335, 2021. <https://doi.org/10.3390/jmse9030335>
- 628 Feistl, T., Bebi, P., Dreier, L., Hanewinkel, M., Bartelt, P.: A coupling of hydrologic  
629 and hydraulic models appropriate for the fast floods of the Gardon river basin  
630 (France). *Natural Hazards & Earth System Sciences*, 14(11), 2899-2920, 2014.  
631 <https://doi.org/10.5194/nhess-14-2899-2014>
- 632 Garcia-Navarro P., Murillo J., Fernandez-Pato J., Echeverribar I., Morales-Hernandez  
633 M.: The shallow water equations and their application to realistic cases.  
634 *Environmental fluid mechanics*. 19(5): 1235-1252, 2019.  
635 <https://doi.org/10.1007/s10652-018-09657-7>
- 636 Ghazizadeh, M.A., Mohammadian, A., Kurganov, A.: An adaptive well-balanced



- 637 positivity preserving central-upwind scheme on quadtree grids for shallow water  
638 equations. *Computers & Fluids*. 208, 104633, 2020,  
639 <https://doi.org/10.1016/j.compfluid.2020.104633>
- 640 Gomes, M.M.D., Verçosa, L.F.D., Cirilo, J.A.: Hydrologic models coupled with 2D  
641 hydrodynamic model for high-resolution urban flood simulation, *Natural Hazards*.  
642 108: 3121-3157, 2021. <https://doi.org/10.1007/s11069-021-04817-3>
- 643 Hu, R., Fang, F., Salinas, P., Pain, C.C.: Unstructured mesh adaptivity for urban  
644 flooding modelling. *Journal of Hydrology* 560,354-363, 2018.  
645 <https://doi.org/10.1016/j.jhydrol.2018.02.078>
- 646 Hou, J., Wang, R., Liang, Q., Li, Z., Huang, M.S., Hinkelmann, R.: Efficient surface  
647 water flow simulation on static cartesian grid with local refinement according to  
648 key topographic features. *Computers & Fluids*, 176, 117-134, 2018.  
649 <https://doi.org/10.1016/j.compfluid.2018.03.024>
- 650 Hou J., Liu F., Tong Y., Guo K., Li D.: Numerical simulation for runoff regulation in  
651 rain garden using 2D hydrodynamic model. *Ecological Engineering*, 153(2),  
652 105794, 2020. <https://doi.org/10.1016/j.ecoleng.2020.105794>
- 653 Hdeib, R., Abdallah, C., Colin, F., Brocca, L., Moussa, R.: Constraining coupled  
654 hydrological-hydraulic flood model by past storm events and post-event  
655 measurements in data-sparse regions, *Journal of Hydrology*, 540 (565), 160-176,  
656 2018. <https://doi.org/10.1016/j.jhydrol.2018.08.008>
- 657 Jaber, F.H., Mohtar, R.H.: Stability and accuracy of two-dimensional kinematic wave  
658 overland flow modeling. *Advances in Water Resources*, 26(11): 1189-1198, 2003.  
659 [https://doi.org/10.1016/S0309-1708\(03\)00102-7](https://doi.org/10.1016/S0309-1708(03)00102-7)
- 660 Kim, J., Warnock, A., Ivanov, V.Y., Katopodes, N.D.: Coupled Modeling of  
661 Hydrologic and Hydrodynamic Processes Including Overland and Channel Flow.



- 662 Advances in Water Resources, 37, 104-126, 2012.  
663 <https://doi.org/10.1016/j.advwatres.2011.11.009>
- 664 Kuffour, B., Engdahl, N.B., Woodward, C.S., Condon, L.E., Kollet, S., Maxwell, R.M.:  
665 Simulating coupled surface–subsurface flows with parflow v3.5.0: capabilities,  
666 applications, and ongoing development of an open-source, massively parallel,  
667 integrated hydrologic model. Geoscientific Model Development, 3, 2020.  
668 <https://doi.org/10.5194/GMD-13-1373-2020>
- 669 Kesserwani, G., Sharifian, M.K.: (Multi)wavelet-based Godunov-type simulators of  
670 flood inundation: Static versus dynamic adaptivity. Advances in water resources,  
671 171,104357, 2023. <https://doi.org/10.1016/j.advwatres.2022.104357>
- 672 Jiang, C., Zhou, Q., Yu, W., Yang, C., Lin, B.: A dynamic bidirectional coupled surface  
673 flow model for flood inundation simulation. Natural Hazards and Earth System  
674 Sciences, 21(2), 497-515, 2021. <https://doi.org/10.5194/nhes-21-497-2021>
- 675 Lai, Y.G.: Watershed runoff and erosion modeling with a hybrid mesh model. Journal  
676 of Hydrologic Engineering, 14(1), 15-26, 2009.  
677 [https://doi.org/10.1061/\(ASCE\)1084-0699\(2009\)14:1\(15\)](https://doi.org/10.1061/(ASCE)1084-0699(2009)14:1(15))
- 678 Moore, I.D., Grayson, R.B., Ladson, A.R.: Digital terrain modelling: a review of  
679 hydrological, geomorphological, and biological applications. Hydrological  
680 Processes, 5(1), 3-30, 1991. <https://doi.org/10.1002/hyp.3360050103>
- 681 Munar, A.M., Cavalcanti, J.R., Bravo, J.M., Fan, F.M., da Motta-Marques, D., Fragos  
682 C.R.: Coupling large-scale hydrological and hydrodynamic modeling: toward a  
683 better comprehension of watershed-shallow lake processes. Journal of Hydrology,  
684 564, 424-441, 2018. <https://doi.org/10.1016/j.jhydrol.2018.07.045>
- 685 Ming, X., Liang, Q., Xia, X., Li, D., Fowler, H.J.: Real-time flood forecasting based on  
686 a high-performance 2-D hydrodynamic model and numerical weather predictions.



- 687 Water Resources Research, 56, e2019WR025583, 2020.  
688 <https://doi.org/10.1029/2019WR025583>
- 689 Morales-Hernández, M., Sharif, M.B., Kalyanapu, A., Ghafoor, S.K., Dullo, T.T.,  
690 Gangrade, S., Kao, S.C., Norman, M.R., Evans, K.J.: Triton: a multi-GPU open  
691 source 2D hydrodynamic flood model. Environmental Modelling and Software,  
692 141,105034, 2021, <https://doi.org/10.1016/j.envsoft.2021.105034>
- 693 Noh, S.J., Lee, J.H., Lee, S., Kawaike, K., Seo, D.J.: Hyper-resolution 1D-2D urban  
694 flood modelling using lidar data and hybrid parallelization. Environmental  
695 Modelling & Software, 103, 131-145, 2018.  
696 <https://doi.org/10.1016/j.envsoft.2018.02.008>
- 697 Ozgen-Xian, I., Kesserwani, G., Caviedes-Voullieme, D., Molins, S., Xu, Z.X.,  
698 Dwivedi, D., Moulton, J.D., Steefel, C.I.: Wavelet-based local mesh refinement  
699 for rainfall-runoff simulations. Journal of Hydroinformatics, 22(5), 1059-1077,  
700 2020. <https://doi.org/10.2166/hydro.2020.198>
- 701 Rossman, L.A. Storm Water Management Model User's Manual Version 5.1;  
702 EPA/600/R-14/413b; U.S. Environmental Protection Agency: Cincinnati, OH,  
703 USA, 2015.
- 704 Schumann, G.J.P., Neal, J.C., Voisin, N., Andreadis, K.M., Pappenberger, F.,  
705 Phanthuwongpakdee, N., Hall, A.C., Bates, P.D.: A first large-scale flood  
706 inundation forecasting model. Water Resource Research 49(10):6248–6257, 2013.  
707 <https://doi.org/10.1002/wrcr.20521>
- 708 Sánchez, R.R.: GIS-Based Upland Erosion Modeling, Geovisualization and Grid Size  
709 Effects on Erosion Simulations with CASC2D-SED. Ph.D. Thesis, Colorado State  
710 University, Fort Collins, CO, USA, 2002.
- 711 Singh J., Altinakar M.S., Yan D.: Two-dimensional numerical modeling of dam-break



- 712 flows over natural terrain using a central explicit scheme. *Advances in Water*  
713 *Resources*, 34(10), 1366-1375, 2011.  
714 <https://doi.org/10.1016/j.advwatres.2011.07.007>
- 715 Shin S., Her Y., Song J.H., Kang M.S.: Integrated sediment transport process modeling  
716 by coupling soil and water assessment tool and environmental fluid dynamics code.  
717 *Environmental Modelling and Software*, 116: 26-39, 2019.  
718 <https://doi.org/10.1016/j.envsoft.2019.02.002>
- 719 Shen, Y., Jiang, C., Zhou, Q., Zhu, D., Zhang, D.: A Multigrid Dynamic Bidirectional  
720 Coupled Surface Flow Routing Model for Flood Simulation. *Water*, 13, 3454,  
721 2021. <https://doi.org/10.3390/w13233454>
- 722 Shen, Y., Jiang, C.: Quantitative assessment of computational efficiency of numerical  
723 models for surface flow simulation. *Journal of Hydroinformatics*, 25 (3): 782–796,  
724 2023. <https://doi.org/10.2166/hydro.2023.131>
- 725 Tarboton, D.G.: A new method for the determination of flow directions and upslope  
726 areas in grid digital elevation models. *Water Resources Research*, 33(2), 662-670,  
727 1997. <https://doi.org/10.1029/96WR03137>
- 728 Toro, E., Spruce, M., Speares, W.: Restoration of the contact surface in the HLL-  
729 Riemann solver. *Shock Waves*, 4, 25-34, 1994.  
730 <https://doi.org/10.1007/BF01414629>
- 731 Toro, E.F.: *Shock-Capturing Methods for Free-Surface Shallow Flows*. John Wiley,  
732 2001.
- 733 Van Leer, B.: Towards the ultimate conservative difference scheme V: A second order  
734 sequel to Godunov's method. *Journal of Computational Physics*, 32(1), 101-136,  
735 1979. [https://doi.org/10.1016/0021-9991\(79\)90145-1](https://doi.org/10.1016/0021-9991(79)90145-1)
- 736 Wing, O., Sampson, C.C., Bates, P.D., Quinn, N., Neal, J.C.: A flood inundation



737 forecast of hurricane Harvey using a continental-scale 2D hydrodynamic model.  
738 Journal of Hydrology X, 4, 100039, 2019.  
739 <https://doi.org/10.1016/j.hydroa.2019.100039>  
740 Yu, W.: Research on Coupling Model of Hydrological and Hydraulics Based on  
741 Adaptive Grid. Ph.D. Thesis, Tsinghua University, Beijing, China, 2019.  
742 Xia, X., Liang, Q, Ming, X.: A full-scale fluvial flood modelling framework based on  
743 a high-performance integrated hydrodynamic modelling system (HiPIMS).  
744 Advances in Water Resources, 132, 103392, 2019.  
745 <https://doi.org/10.1016/j.advwatres.2019.103392>